RSC Advances

PAPER

View Article Online
View Journal | View Issue

Cite this: *RSC Adv.*, 2015, **5**, 81438

Microwave-assisted synthesis of hematite/activated graphene composites with superior performance for photocatalytic reduction of Cr(VI)†

Yuanxin Du,[a] Zhuchen Tao,[a] Jian Guan,[a] Zijun Sun,[a] Wencong Zeng,[a] Pengchao Wen,[a] Kun Ni,[a] Jianglin Ye,[a] Shangfeng Yang,[a] Pingwu Du[ab] and Yanwu Zhu*[ab]

Received 4th August 2015
Accepted 4th September 2015

DOI: 10.1039/c5ra15561d

www.rsc.org/advances

Hematite (α-Fe_2O_3) nanoparticles are deposited onto porous 'activated microwave expanded graphite oxide' (aMEGO) carbon *via* a simple, rapid one-pot microwave process. Under the irradiation of visible light, the α-Fe_2O_3/aMEGO composites exhibit significantly enhanced photocatalytic activity for the reduction of Cr(VI) to Cr(III). A maximum Cr(VI) removal rate of 95.28% is obtained for the composite containing 7.72 wt% aMEGO as compared to that of 25.26% for pure α-Fe_2O_3; the rate constant of the composite is nearly 9 times higher than that of pure α-Fe_2O_3. The crucial role of aMEGO in enhancing the photocatalytic efficiency of the composites relies not only on its large surface area, but also on the high conductivity which benefits the transport of photoexcited electrons. The enhancement in the charge separation and the suppression in the electron–hole pair recombination is evidenced by an increased photocurrent and a suppressed photoluminescence in the α-Fe_2O_3/aMEGO composites.

Introduction

Unlike most organic pollutants, heavy metal contaminants are especially dangerous and bothersome because they are non-biodegradable and tend to accumulate in living tissues throughout the food chain.[1] In particular, hexavalent chromium (Cr(VI)) is a contaminant frequently found in wastewater from industrial processes such as electroplating, metal finishing, leather tanning, paint making, textile production and dyeing, *etc.*[2] Due to its high toxicity, mutagenic and carcinogenic activity towards human beings, and extremely high solubility and mobility in water, Cr(VI) has been listed as one of the primary pollutants by the United States Environmental Protection Agency; its allowable content in drinking water has been strictly regulated as 0.05 mg l^{-1} by the World Health Organization.[3] Hence, how to efficiently and economically treat Cr(VI)-containing water has been a challenging topic for both academia and industry. Various techniques such as chemical precipitation,[4] reverse osmosis,[5] ion exchange,[6] foam flotation,[7] electrolysis,[8] adsorption[9] and photocatalytic reduction[3,10] have been investigated for Cr(VI) removal. Among these methods, photocatalytic reduction can efficiently convert Cr(VI) to Cr(III), which is considered as a nontoxic and essential trace metal in human nutrition within a certain limit,[10] and can be readily precipitated as $Cr(OH)_3$ in neutral or alkaline solutions for removal as solid waste.[3]

A broad range of semiconductors such as TiO_2, ZnO, CdS, SnS_2, In_2S_3 and so on have been developed as photocatalysts to reduce Cr(VI) to Cr(III).[2,3,10–14] On the other hand, its cost-effective, chemically stable and environmentally benign features make α-Fe_2O_3 a promising candidate for an efficient photocatalyst.[15,16] α-Fe_2O_3 has a narrow bandgap (1.9–2.2 eV) which can be utilized to absorb visible light, a substantial fraction of the solar spectrum. The poor conductivity and the short-hole diffusion length, however, has resulted in a quick recombination of photo-induced electron–hole pairs in α-Fe_2O_3 and thus restricted its practical applications in photocatalysis.[17–20] A variety of studies have been attempted to overcome these obstacles, utilizing strategies such as metal[21,22] and non-metal doping[23,24] or the formation of composites with carbon quantum dots.[25] To the best of our knowledge, there has been no report published on α-Fe_2O_3 composites for the reduction of Cr(VI).

Carbon is more chemically stable than metals and potentially has a high ion adsorption efficiency. As a two dimensional (2D) allotrope of carbon with a potentially high carrier mobility,[26] graphene has been combined with α-Fe_2O_3, *e.g.* by hydrothermal methods,[17,18] to form hybrid materials for improved photocatalytic performance in treating organic

---

[a] *Key Laboratory of Materials for Energy Conversion, Chinese Academy of Sciences, Department of Materials Science and Engineering, University of Science and Technology of China, 96 Jin Zhai Rd, Hefei, Anhui Province, 230026, P. R. China. E-mail: zhuyanwu@ustc.edu.cn*

[b] *iChEM (Collaborative Innovation Center of Chemistry for Energy Materials), University of Science and Technology of China, 96 Jin Zhai Rd, Hefei, Anhui Province, 230026, P. R. China*

† Electronic supplementary information (ESI) available. See DOI: 10.1039/c5ra15561d

pollutants. Pradhan *et al.*[18] reported a synthesis of α-Fe_2O_3 nanorod/reduced graphene oxide (RGO) composites which showed a 4-fold enhancement in photodegradation efficiency for phenol compared with pure α-Fe_2O_3 nanorods. Han *et al.*[17] reported α-Fe_2O_3 nanoplate/RGO composites, based on which the rate constant is also four times higher than that of pure α-Fe_2O_3 nanoplates for the degradation of Rhodamine B (RhB). These efforts suggested that α-Fe_2O_3/graphene composites have the potential to significantly enhance the photocatalytic activity for the degradation of organic pollutants. However, the time-consuming synthesis, the poor conductivity due to the incomplete reduction of GO and the difficulty in recycling of the photocatalysts, may restrict the applications of α-Fe_2O_3/RGO catalysts. In addition, the restacking of RGO nanoplates derived from GO limits the adsorption of pollutants and thus deteriorates the performance. Ideally, a three-dimensional (3D) porous graphene structure with both high surface area and high electrical conductivity may act as an excellent support for photocatalysts, probably leading to the desired photocatalytic efficiency and recyclability for the reduction of ions like Cr(VI).

In our previous work[27] a porous carbon structure called 'activated microwave expanded graphite oxide' (aMEGO) was reported to have a large surface area of up to 3100 $m^2\ g^{-1}$ and a high electrical conductivity. In the present work, α-Fe_2O_3/aMEGO composites were synthesized by a simple and rapid microwave process. The effects of aMEGO content in the composite on the structure, morphology, optical properties, photocurrent and photocatalytic properties of the α-Fe_2O_3/aMEGO composites were systematically investigated. In particular, for an optimal content of 7.72 wt% aMEGO in the composite, the photodegradation rate constant for the reduction of Cr(VI) to Cr(III) for the composites reaches 9 times higher than that of pure α-Fe_2O_3. With a cost-effective synthesis, the current work provides a potentially useful strategy for other semiconductor/aMEGO composites with superior photocatalytic activity.

Experimental section

Sample preparation

The synthesis of aMEGO was performed by following the method described in ref. 27. For the synthesis of the α-Fe_2O_3/aMEGO composites, aMEGO powder was suspended in ultra-pure water (2 mg ml^{-1}) and ultrasonicated (250 W) for 1 h. Then various amounts of iron(III) nitrate nonahydrate ($Fe(NO_3)_3\cdot 9H_2O$) was added to the suspension, and the mixture suspension was stirred using vacuum impregnation for 3 h. After being dried in a vacuum oven at 60 °C for 12 h, the mixture was placed into a domestic microwave oven for exposure to microwaves. The exposure duration and microwave power were 180 s and 500 W, respectively. The composites with aMEGO to α-Fe_2O_3 ratios of 2 : 98, 5 : 95, 8 : 92, 10 : 90 (calculated based on the amount of aMEGO and $Fe(NO_3)_3\cdot 9H_2O$ added) were obtained and labeled as α-Fe_2O_3/aMEGO-1, α-Fe_2O_3/aMEGO-2, α-Fe_2O_3/aMEGO-3 and α-Fe_2O_3/aMEGO-4, respectively. For comparison, pure α-Fe_2O_3 was also obtained by direct microwave-assisted heating of $Fe(NO_3)_3\cdot 9H_2O$, the exposure duration and microwave power were 180 s and 500 W, respectively. All the chemicals were purchased from Sigma and used without further purification.

Characterization

The morphology, structure and composition of the samples were characterized using scanning electron microscopy (SEM, JSM-6700F), high-resolution transmission electron microscopy (HRTEM, JEOL 2010), and X-ray diffraction spectroscopy (XRD, D/max-TTR III) with Cu Kα radiation ($V = 40$ kV, $I = 200$ mA), respectively. The scanning rate in XRD was 5° min^{-1} from 10° to 80° (2θ). Fourier transform infrared spectroscopy (FTIR, NICOLET 8700), Raman spectroscopy (Renishaw inVia Raman Microscope, 532 nm laser, 5 mW) and X-ray photoelectron spectroscopy (XPS, ESCALAB 250) were performed to further characterize the chemical components in the composites. Thermogravimetry (TG) analysis of the samples was carried out in air using a TGA Q5000 with a heating rate of 5 °C min^{-1}. The specific surface areas were measured by nitrogen adsorption–desorption using a TriStar II 3020M with the Brunauer–Emmett–Teller (BET) method.

The absorption and fluorescence spectra of the samples were taken at room temperature with a UV-visible spectrophotometer (Shimadzu Solid 3700 spectrometer) and a photoluminescence (PL) spectrofluorometer (JY Fluorolog-3-Tou) with an excitation light at 350 nm, respectively. The equation $(\alpha h\nu) = A(h\nu - E_g)^n$ was used to estimate the band gap energy of all catalysts, where α, ν, A, and E_g are the absorption coefficient, light frequency, proportionality constant and band gap energy, respectively; n describes the type of transition in a semiconductor, that is $n = 1/2$ for a direct transition and $n = 2$ for an indirect transition.[18,28] The value of n for all the synthesized samples in this work was taken as 1/2, since the direct optical transition in the α-Fe_2O_3/aMEGO composites is allowed.[18] Photocurrent measurements were performed on a CHI 602E electrochemistry potentiostat in a standard three-electrode configuration with a photocatalyst-coated ITO glass as the working electrode, an Ag/AgCl as the reference electrode, and a Pt plate as the counter electrode. In the photocurrent measurements light irradiation was provided by a 300 W xenon lamp with a cutoff filter ($\lambda > 420$ nm). Sodium sulfate (Na_2SO_4, 0.5 M) solution was used as the electrolyte. To do the photocurrent measurements, 10 μl of slurry, which was made by dispersing 10 mg of α-Fe_2O_3 or α-Fe_2O_3/aMEGO in 0.5 ml of H_2O followed by sonication for 2 h, was dip-coated onto the ITO working electrodes and dried at room temperature. The scan rate was 50 mV s^{-1}, and all the potentials are presented relative to Ag/AgCl.

Photocatalytic evaluation

The photocatalytic performance of α-Fe_2O_3 or α-Fe_2O_3/aMEGO was evaluated by the photocatalytic reduction of Cr(VI) under visible light irradiation. The catalyst sample was dispersed in 50 ml Cr(VI) solutions (10 mg l^{-1}) prepared by dissolving $K_2Cr_2O_7$ in deionized water to a catalyst concentration of 1 mg ml^{-1}. At pH = 2, the mixed suspension was first magnetically stirred in the dark for 30 min to reach the adsorption–desorption equilibrium. After that, the mixed suspension was exposed to visible light produced by the 300 W xenon lamp ($\lambda > 420$ nm) under continuous stirring. At certain time intervals, 4 ml of the mixed suspensions was extracted and centrifuged to remove the extra photocatalyst. Then the Cr(VI) content in the solution was determined colorimetrically at 540 nm using the diphenylcarbazide (DPC) method.[10] The reduction ratio (R_r) of Cr(VI) was calculated from the measured absorbance intensity after a certain duration of illumination with the following expression:

$$R_r = (A_0 - A_t)/A_0 \times 100\%,$$

where A_0 and A_t are the absorbance intensities of the sample taken when being illuminated for 0 min (measured right after the adsorption in dark but before the illumination) and t min of illumination, respectively.

Results and discussion

Scheme 1 illustrates a possible structure of a α-Fe_2O_3/aMEGO composite, in which α-Fe_2O_3 nanoparticles are attached to the matrix of highly porous aMEGO, as verified below. With extremely high specific surface areas of up to 3100 $m^2\ g^{-1}$ and essentially 100% sp^2 carbon, aMEGO is presumably considered as a continuous 3D network of highly curved atom-thick carbons.[27] aMEGO has been used as an electrically conductive scaffold for hosting MnO_2 for superior energy storage.[29] Under visible light irradiation, electrons in α-Fe_2O_3 are excited and electron–hole pairs are generated. Cr(VI) is reduced to Cr(III) by photogenerated electrons, while water molecules are oxidized by the holes to oxygen.[28,30–35] In addition, due to the high porosity and large surface area of aMEGO, the composite could potentially offer more adsorption sites active to reactants around the α-Fe_2O_3 nanoparticles and thus might enhance the catalytic reaction. Meanwhile, the excellent conductivity of aMEGO allows more efficient electron–hole separation and thus prolongs the lifetime of the charge carriers, further promoting the photocatalytic activity.

The SEM and HRTEM images in Fig. 1A and B show the typical morphology of aMEGO and the 3D distribution of meso- and micropores as reported previously.[27] Below, α-Fe_2O_3/aMEGO-3 will be discussed as a representative of the composites due to the optimized photocatalytic performance. After a rapid one-pot microwave reaction, it is clearly observed that aMEGO has been densely and uniformly decorated with α-Fe_2O_3 spherical nanoparticles as shown in the SEM and TEM images in Fig. 1C and D. The typical size of the nanoparticles shown in Fig. 1D is about 20 nm, bigger than the average pore size of aMEGO,[27] suggesting that most nanoparticles observed here are attached to the surface of aMEGO. It is worth noting that even after 30 min of sonication for the preparation of the TEM specimen, aMEGO is still a stable support for the anchoring of α-Fe_2O_3 nanoparticles, indicated by the strong combination between aMEGO and α-Fe_2O_3.[17,18] The actual content of aMEGO in the as-synthesized composites has been determined as 2.14, 6.38, 7.72 or 11.36 wt% for α-Fe_2O_3/aMEGO-1, α-Fe_2O_3/aMEGO-2, α-Fe_2O_3/aMEGO-3 or α-Fe_2O_3/aMEGO-4, respectively, using thermogravimetry (TG) analysis (Fig. S1†). The difference in the aMEGO content from the originally calculated ratios could be partially explained by the loss of aMEGO in the process of the microwave reaction. TEM images of α-Fe_2O_3/aMEGO-1, α-Fe_2O_3/aMEGO-2 and α-Fe_2O_3/aMEGO-4 are displayed in Fig. S2.† For α-Fe_2O_3/aMEGO-1 with a low content of aMEGO, the apparent aggregation of nanoparticles is observed, while the distribution of α-Fe_2O_3 nanoparticles is sparser as the aMEGO content increases. The HRTEM image in Fig. 1E indicates the crystalline nature of the α-Fe_2O_3 nanoparticles in α-Fe_2O_3/aMEGO-3. The lattice fringes are clearly observed with spacings of 0.25 nm and 0.27 nm, corresponding

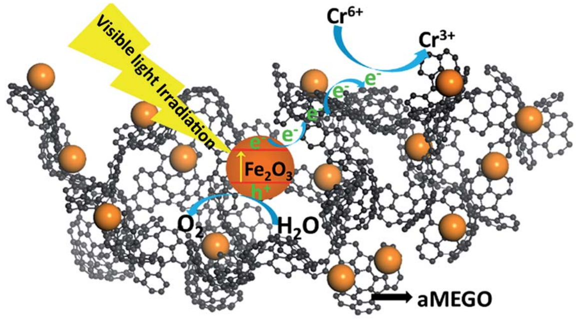

Scheme 1 Schematic illustration for the photocatalytic reduction of Cr(VI) with α-Fe_2O_3/aMEGO composites under visible light irradiation.

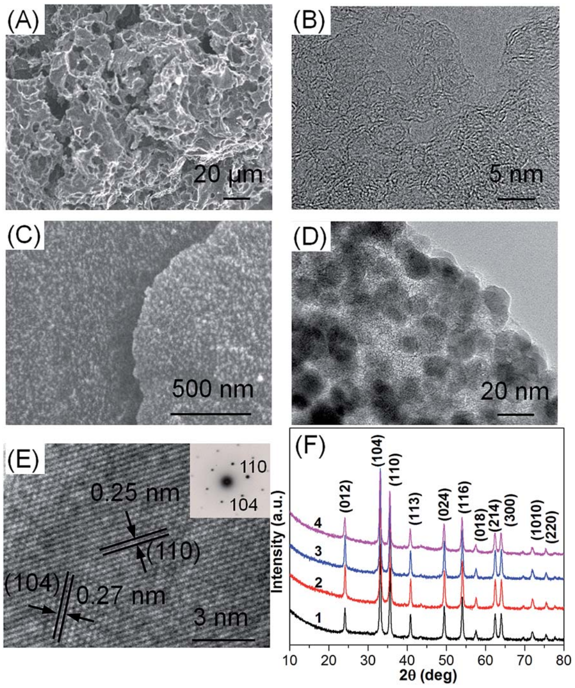

Fig. 1 (A) SEM and (B) TEM images of aMEGO; (C) SEM and (D) TEM images of α-Fe_2O_3/aMEGO-3; (E) HRTEM image of α-Fe_2O_3/aMEGO-3. The inset is the corresponding SAED pattern of the α-Fe_2O_3 nanoparticles; (F) XRD patterns of α-Fe_2O_3/aMEGO-1 (curve 1), α-Fe_2O_3/aMEGO-2 (curve 2), α-Fe_2O_3/aMEGO-3 (curve 3) and α-Fe_2O_3/aMEGO-4 (curve 4).

to the interspatial distance of the (110) and (104) planes of α-Fe_2O_3 and consistent with the selected area electron diffraction (SAED) pattern (inset of Fig. 1E). The X-ray diffraction (XRD) patterns shown in Fig. 1F further confirm that the single-crystal hematite structure (JCPDS card no. 33-0664) is seen for all α-Fe_2O_3/aMEGO composites with different amounts of aMEGO. No typical diffraction peaks of aMEGO were detected, probably due to the low amount of aMEGO in the composites and the amorphous structure of aMEGO (Fig. S3A†), similar to other semiconductor/RGO composites.[17,28,36]

The elemental compositions of the α-Fe_2O_3/aMEGO composites were characterized using X-ray photoelectron spectroscopy (XPS) analysis. The C 1s XPS spectrum (Fig. 2A) reveals four components at 284.78, 286.21, 287.55 and 289.07 eV corresponding to a C–C bond with an sp^2 orbital, C–O, C=O and COOH functional groups, respectively. The presence and locations of these peaks are in good agreement with those of aMEGO (Fig. S3B†). The O 1s spectrum is shown in Fig. 2B. The broad peak between 528 eV and 535 eV could be deconvoluted into four peaks: an Fe–O signal appears at 529.80 eV, whereas the other peaks result from oxygen-containing groups in aMEGO (Fig. S3C†), such as C=O at 531.35 eV, C–O at 532.48 eV and C–OH at 533.37 eV.[25] The Fe 2p spectrum in Fig. 2C can be fitted to two peaks at 711.11 and 724.60 eV corresponding to the $2p_{3/2}$ and $2p_{1/2}$ spin–orbital components (with a spin energy separation of 13.49 eV due to the spin–orbit coupling), respectively. A clearly distinguishable satellite peak located at 719 eV, approximately 8 eV higher than the main Fe $2p_{3/2}$ peak of α-Fe_2O_3, does not overlap with either the Fe $2p_{3/2}$ or Fe $2p_{1/2}$ peak.[25,37] It can be solely attributed to the presence of the Fe^{3+} ions in α-Fe_2O_3 and all these peaks confirm the presence of hematite in the composites (compared with Fig. S3D†).

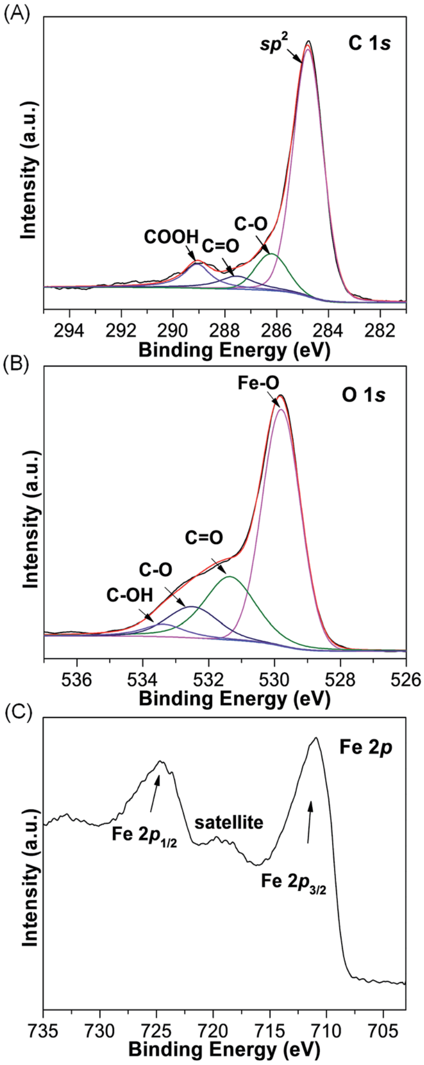

Fig. 2 XPS spectra of α-Fe_2O_3/aMEGO-3: (A) C 1s spectrum, (B) O 1s spectrum and (C) Fe 2p spectrum.

Fourier transform infrared (FT-IR) spectroscopy was used to compare the chemical structure of the pure aMEGO and the α-Fe_2O_3/aMEGO composites. As shown in Fig. 3A, the FT-IR spectrum of aMEGO exhibits a broad band over the range of 3100–3600 cm^{-1}, associated with the stretching modes of hydroxy (–OH) groups. Other bands at ~2945 cm^{-1}, ~1634 cm^{-1} and ~1095 cm^{-1} are assigned to the sp^3 C–H stretching, the aromatic C=C and the C–O stretching vibration of the COOH groups.[17,25,38] In comparison, α-Fe_2O_3/aMEGO-3 shows nearly the same characteristic peaks as aMEGO and the strong peaks at 570 cm^{-1} and 480 cm^{-1} are attributed to Fe–O vibrations, in agreement with those observed for the hematite particles.[25,38] These results suggest that the chemical environment in aMEGO remains unchanged while the α-Fe_2O_3 nanoparticles are incorporated with aMEGO. The Raman spectrum of aMEGO in Fig. 3B shows two characteristic peaks at 1339 and 1589 cm^{-1}, corresponding to the breathing mode of the *k*-point phonons of A_{1g} symmetry associated with the disorder and defects in graphene (D band) and the first-order scattering of the E_{2g} phonon of the sp^2 carbon atoms of graphene (G band), respectively.[17] In the Raman spectrum of α-Fe_2O_3/aMEGO-3, the peaks at 215, 283 and 398 cm^{-1} are identified as the $A_{1g}(1)$, $E_g(2)$ and $E_g(4)$ of hematite.[37] Compared with the G peak located at 1589 cm^{-1} in aMEGO, the G peak in α-Fe_2O_3/aMEGO-3 has shifted to 1603 cm^{-1}, due to the charge transfer from aMEGO to α-Fe_2O_3, as found in other graphene based composites.[39,40] The D peak of aMEGO overlaps with the magnon scattering of α-Fe_2O_3 (Fig. S4†), which makes the possible shift hard to distinguish.[39] The same I(D)/I(G) intensity ratio for aMEGO (1.211) and α-Fe_2O_3/aMEGO-3 (1.207) suggests that the introduction of α-

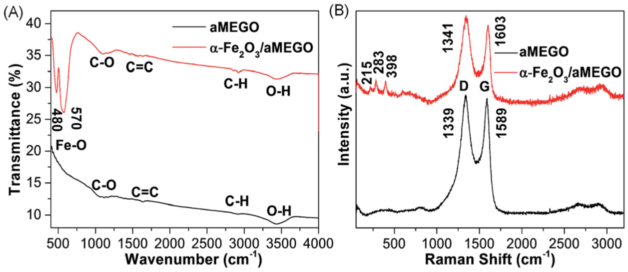

Fig. 3 FT-IR spectra (A) and Raman spectra (B) of aMEGO and α-Fe_2O_3/aMEGO-3.

Fe_2O_3 has no significant influence on the defects and disorders in aMEGO.

The photocatalytic properties of the α-Fe_2O_3/aMEGO composites were evaluated by the reduction of Cr(VI) under visible light irradiation. To rule out the contribution from the physical adsorption in aMEGO-containing composites, 30 min of dark stirring was carried out to reach the adsorption–desorption equilibrium, as shown in Fig. S5.† Fig. 4A shows the photocatalytic reduction of Cr(VI) by α-Fe_2O_3/aMEGO-3 through the temporal evolution spectra, from which we can clearly see the characteristic absorption peak at 540 nm decreases in intensity as the time is prolonged. The variation in the degree of Cr(VI) degradation (C/C_0, where C_0 and C are the initial concentration after the dark adsorption and the residual concentration at a certain reaction time, respectively) with irradiation duration is shown in Fig. 4B. Pure α-Fe_2O_3 shows a Cr(VI) reduction ratio of about 25.26% after 160 min of continuous irradiation. With the introduction of aMEGO, the reduction ratio of the composites has been greatly enhanced to 95.28% for α-Fe_2O_3/aMEGO-3, after 160 min of visible light illumination. However, a further increase in the aMEGO content, *e.g.* to 11.36 wt% in α-Fe_2O_3/aMEGO-4, leads to a little decrease in the photocatalytic activity, as also observed in other graphene based photocatalysts.[17,18,28] We also investigated the factors affecting the photocatalytic activity which include the adsorption capacity of pores, the light absorption ability, the carrier separation and recombination efficiency as stated hereinafter. On the other hand, the rate constant k, a basic kinetics parameter reflecting the reaction rate of the photocatalytic process, was calculated from the pseudo first order kinetics equation $\ln(C_0/C) = kt$, where t is the reaction time.[17] From the curves of $\ln(C_0/C)$ *versus* t displayed in Fig. 4C, the highest value of $k = 0.01829\ \text{min}^{-1}$ is obtained from α-Fe_2O_3/aMEGO-3, nearly 9 times higher than that of pure α-Fe_2O_3. In comparison, α-Fe_2O_3/RGO composites showed only a 4-fold enhancement in degradation efficiency for phenol or RhB over that of pure α-Fe_2O_3.[17,18] We have also compared the Cr(VI) reduction efficiency of α-Fe_2O_3/aMEGO with those of other graphene-based semiconductor photocatalysts obtained under the optimal conditions for each. As can be seen from Table S1,† α-Fe_2O_3/aMEGO-3 has demonstrated one of the best performances under visible irradiation among various graphene-based photocatalytic composites in terms of Cr(VI) reduction efficiency.

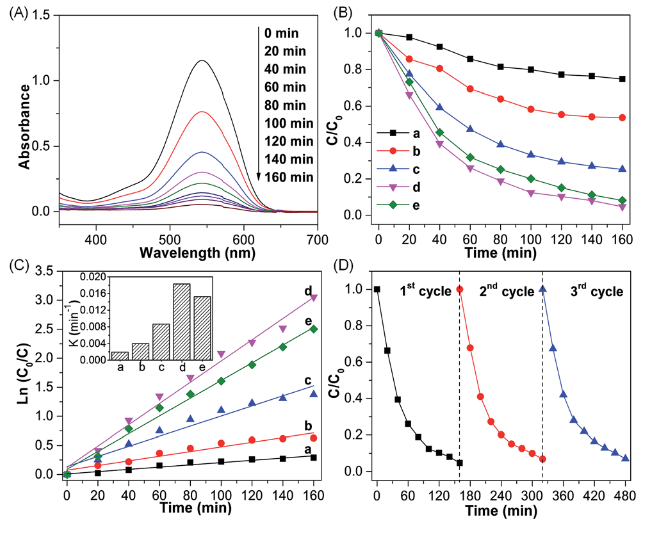

Fig. 4 (A) Time-dependent UV-vis absorption spectra of DPC-Cr(VI) complex solutions in the presence of α-Fe_2O_3/aMEGO-3 under visible light irradiation. (B) Photocatalytic reduction of aqueous Cr(VI) and (C) kinetic curves of the degradation process by (a) α-Fe_2O_3, (b) α-Fe_2O_3/aMEGO-1, (c) α-Fe_2O_3/aMEGO-2, (d) α-Fe_2O_3/aMEGO-3 and (e) α-Fe_2O_3/aMEGO-4 under visible light irradiation. The inset of (C) is the corresponding rate constant. (D) Cyclic photocatalytic reduction of aqueous Cr(VI) by α-Fe_2O_3/aMEGO-3.

The stability of α-Fe_2O_3/aMEGO-3 was further investigated by performing recycling tests under identical conditions. As shown in Fig. 4D, the photocatalytic activity of α-Fe_2O_3/aMEGO-3 slightly decreases from 95.28% for the first cycle to 93.25% or 93.02% for the second or third circles, respectively. As shown in Fig. S6,† the XRD pattern and SEM image of α-Fe_2O_3/aMEGO-3 after three cycles show that the catalyst maintains the structure and morphology from before cycling. The results indicate that the α-Fe_2O_3/aMEGO composites can be used as highly efficient and stable visible light photocatalysts for Cr(VI) reduction in water.

To obtain hints about the mechanisms for the superior performance of the α-Fe_2O_3/aMEGO composites, the effect of specific surface area has been investigated. Brunauer–Emmett–Teller (BET) surface areas calculated from the nitrogen adsorption–desorption isotherms (Fig. S7†) of α-Fe_2O_3 and α-Fe_2O_3/aMEGO composites are shown in Fig. 5A. Clearly, the introduction of aMEGO increased the surface area from 14.79 $m^2\ g^{-1}$ for α-Fe_2O_3 to above 120.50 $m^2\ g^{-1}$ for the α-Fe_2O_3/aMEGO-3 and α-Fe_2O_3/aMEGO-4 samples. With high specific surface areas and highly curved 3D carbon networks, aMEGO is used here as a porous carrier without catalytic capacity (Fig. S8†). The enhanced surface area of the α-Fe_2O_3/aMEGO composites could offer more active adsorption sites to adsorb more reactant around the catalyst and thus speed up the catalytic reaction. In addition, the optical absorption properties of the composite catalysts were investigated using UV-vis diffuse reflectance spectra (DRS), as shown in Fig. 5B. α-Fe_2O_3 shows an absorption band at 526 nm corresponding to the $2(^6A_1) \rightarrow (^4T_1)$ ligand field transition of Fe^{3+},[18,28] while all the aMEGO-loaded photocatalysts showed a larger absorption edge, which is caused by the blackbody property of aMEGO. The band gap estimated from the plot of $(\alpha h\nu)^n$ *versus* $h\nu$ is shown in the inset of Fig. 5B. The band gap has been reduced by introducing aMEGO into the composite, possibly leading to a higher and wider adsorption of visible light.

The photoelectrochemical properties of the photocatalysts were investigated using photocurrent measurements, as shown in Fig. 5C. As can be seen, the α-Fe_2O_3/aMEGO composite electrodes generate much higher currents than the α-Fe_2O_3 electrode under the same applied potential without light irradiation (Fig. 5C, lines a′–e′). All samples show increased currents when the light is on, and the α-Fe_2O_3/aMEGO composites show higher currents compared to α-Fe_2O_3 (Fig. 5C,

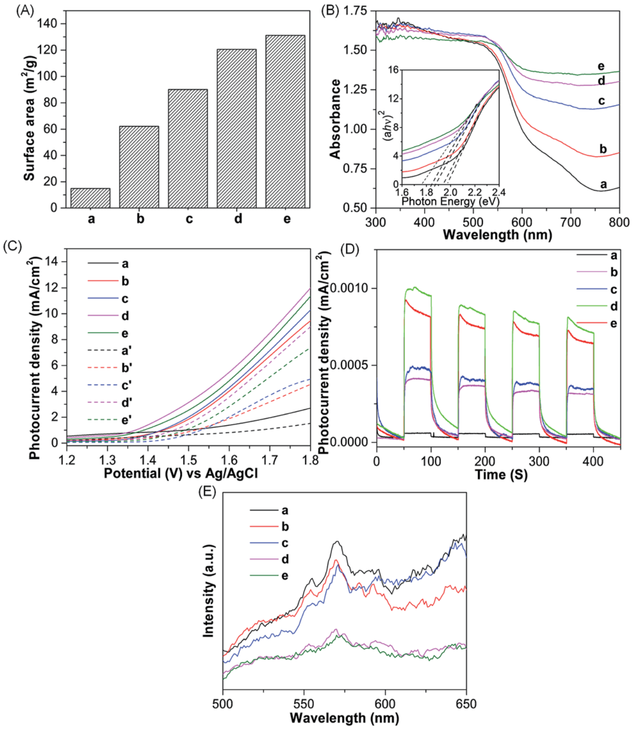

Fig. 5 (A) Surface area and (B) UV-vis absorption spectra for α-Fe_2O_3 and the α-Fe_2O_3/aMEGO composites. The inset in (B) is the corresponding Tauc plot analysis of the optical band gap of the direct transition. (C) Linear sweep voltammagrams with (a–e) and without (a′–e′) visible light irradiation. (D) Amperometric I–t curves with an electrode potential of 0.6 V *versus* Ag/AgCl with 50 s visible light on/off cycles. (E) PL spectra. In all figures (a) α-Fe_2O_3, (b) α-Fe_2O_3/aMEGO-1, (c) α-Fe_2O_3/aMEGO-2, (d) α-Fe_2O_3/aMEGO-3 and (e) α-Fe_2O_3/aMEGO-4.

lines a–e). The current is enhanced with the increase in the content of aMEGO, except for α-Fe_2O_3/aMEGO-4. Fig. 5D shows the time response of the photocurrent for the catalysts by switching the visible light illumination on and off sequentially. It can be seen that the α-Fe_2O_3/aMEGO-3 composite has the highest photocurrent transient response among the five samples studied, suggesting the remarkably efficient separation of charge carriers, which is in agreement with the highest photoactivity of α-Fe_2O_3/aMEGO-3 toward the reduction of Cr(VI).

The separation of charge carriers was also investigated with photoluminescence (PL). Since PL emission results from the radiative recombination of excited electrons and holes it has been a widely-used technique to study the charge carrier transfer process as well as the recombination process of the electron–hole pairs in semiconductors.[17] As demonstrated in other graphene-based photocatalysts, such as α-Fe_2O_3 nanoplate/RGO,[17] α-Fe_2O_3 nanorod/RGO,[18] and α-FeOOH nanorod/RGO,[28] *etc.*, PL displays a significant weakening after RGO is introduced. Similarly, Fig. 5E shows that after aMEGO is combined with α-Fe_2O_3, the PL intensity of the composites decreases rapidly. The PL quenching further confirms the role of aMEGO in inhibiting the electron–hole pair recombination, which is considered to highly contribute to the outstanding photocatalytic performance of the α-Fe_2O_3/aMEGO composites. In Fig. 5E, we find that with the increase in the content of aMEGO (from 2.14 wt% in α-Fe_2O_3/aMEGO-1 to 7.72 wt% in α-Fe_2O_3/aMEGO-3), the PL intensity of the composites reduces gradually; while the PL intensity of the composites remains almost the same when the aMEGO content further increases from 7.72 wt% in α-Fe_2O_3/aMEGO-3 to 11.36 wt% in α-Fe_2O_3/aMEGO-4. This implies that the suppression efficiencies of the photogenerated electron–hole pair recombination in α-Fe_2O_3/aMEGO-3 and α-Fe_2O_3/aMEGO-4 are almost the same.

The results above have clearly shown that the synergistic effect between aMEGO and α-Fe_2O_3 leads to the best photocatalytic efficiency through balancing the contributions of photo absorption, physical adsorption and charge separation, *e.g.* in α-Fe_2O_3/aMEGO-3. Such a combined effect may also explain why a further increase in aMEGO content, *e.g.* in α-Fe_2O_3/aMEGO-4, results in only a little decrease in photocatalytic activity, as also observed in other graphene based photocatalysts.[17,18,28]

Conclusions

In summary, highly active α-Fe_2O_3/aMEGO composites with tunable content of aMEGO were prepared using a simple, rapid, one-pot microwave process. The introduction of aMEGO led to larger surface areas, enhanced light absorption, faster transfer of photoexcited electrons and more efficient separation of photo-generated electron–hole pairs. As a consequence, α-Fe_2O_3/aMEGO-3 with an optimal content of aMEGO achieves a high Cr(VI) removal rate of 95.28% under visible light irradiation, compared to 25.26% for pure α-Fe_2O_3. The rate constant has been enhanced nearly 9-fold. The synergistic effects between α-Fe_2O_3 and aMEGO may lead to the development of low-cost, safe and green α-Fe_2O_3/aMEGO composites potentially useful for treating wastewater.

Acknowledgements

This work was supported by the China Government 1000 Plan Talent Program, the China MOE NCET Program, the NSFC Program (51322204) and the Fundamental Research Funds for the Central Universities (WK2060140014, WK2060140014).

Notes and references

1 C. E. Barrera-Díaz, V. Lugo-Lugo and B. Bilyeu, *J. Hazard. Mater.*, 2012, **223**, 1–12.
2 C. Mondal, M. Ganguly, J. Pal, A. Roy, J. Jana and T. Pal, *Langmuir*, 2014, **30**, 4157–4164.
3 Z. Jin, Y. X. Zhang, F. L. Meng, Y. Jia, T. Luo, X. Y. Yu, J. Wang, J. H. Liu and X. J. Huang, *J. Hazard. Mater.*, 2014, **276**, 400–407.
4 M. Gheju and I. Balcu, *J. Hazard. Mater.*, 2011, **196**, 131–138.
5 L. Cui, Q. Meng, J. Zheng, X. Wei and Z. Ye, *Vacuum*, 2013, **89**, 1–6.

6 Y. Deng, T. Long, H. Zhao, L. Zhu and J. Chen, *Sep. Sci. Technol.*, 2012, **47**, 256–263.

7 A. I. Zouboulis, N. K. Lazaridis and D. Zamboulis, *Sep. Sci. Technol.*, 1994, **29**, 385–400.

8 H. Sarahney, X. Mao and A. N. Alshawabkeh, *Electrochim. Acta*, 2012, **86**, 96–101.

9 W. Li, Y. Tang, Y. Zeng, Z. Tong, D. Liang and W. Cui, *Chem. Eng. J.*, 2012, **193**, 88–95.

10 Y. C. Zhang, J. Li, M. Zhang and D. D. Dionysiou, *Environ. Sci. Technol.*, 2011, **45**, 9324–9331.

11 C. Wang, M. Cao, P. Wang, Y. Ao, J. Hou and J. Qian, *Appl. Catal., A*, 2014, **473**, 83–89.

12 X. Liu, L. Pan, Q. Zhao, T. Lv, G. Zhu, T. Chen, T. Lu, Z. Sun and C. Sun, *Chem. Eng. J.*, 2012, **183**, 238–243.

13 X. Liu, L. Pan, T. Lv, G. Zhu, Z. Sun and C. Sun, *Chem. Commun.*, 2011, **47**, 11984–11986.

14 X. An, C. Y. Jimmy, F. Wang, C. Li and Y. Li, *Appl. Catal., B*, 2013, **129**, 80–88.

15 X. Zhou, J. Lan, G. Liu, K. Deng, Y. Yang, G. Nie, J. Yu and L. Zhi, *Angew. Chem., Int. Ed.*, 2012, **124**, 182–186.

16 H. Liang, X. Xu, W. Chen, B. Xu and Z. Wang, *CrystEngComm*, 2014, **16**, 959–963.

17 S. Han, L. Hu, Z. Liang, S. Wageh, A. A. Al-Ghamdi, Y. Chen and X. Fang, *Adv. Funct. Mater.*, 2014, **24**, 5719–5727.

18 G. K. Pradhan, D. K. Padhi and K. M. Parida, *ACS Appl. Mater. Interfaces*, 2013, **5**, 9101–9110.

19 C. Jorand Sartoretti, B. D. Alexander, R. Solarska, I. A. Rutkowska, J. Augustynski and R. Cerny, *J. Phys. Chem. B*, 2005, **109**, 13685–13692.

20 M. Zhang, Y. Lin, T. J. Mullen, W. F. Lin, L. D. Sun, C. H. Yan, T. E. Patten, D. Wang and G. Y. Liu, *J. Phys. Chem. Lett.*, 2012, **3**, 3188–3192.

21 W. Cheng, J. He, Z. Sun, Y. Peng, T. Yao, Q. Liu, Y. Jiang, F. Hu, Z. Xie and S. Wei, *J. Phys. Chem. C*, 2012, **116**, 24060–24067.

22 A. J. Frierdich, M. M. Scherer, J. E. Bachman, M. H. Engelhard, B. W. Rapponotti and J. G. Catalano, *Environ. Sci. Technol.*, 2012, **46**, 10031–10039.

23 T. H. Jeon, W. Choi and H. Park, *J. Phys. Chem. C*, 2011, **115**, 7134–7142.

24 W. Yan, H. Fan and C. Yang, *Mater. Lett.*, 2011, **65**, 1595–1597.

25 B. Y. Yu and S. Y. Kwak, *J. Mater. Chem.*, 2012, **22**, 8345–8353.

26 K. S. Novoselov, A. K. Geim, S. V. Morozov, D. Jiang, Y. Zhang, S. V. Dubonos, I. V. Grigorieva and A. A. Firsov, *Science*, 2004, **306**, 666–669.

27 Y. Zhu, S. Murali, M. D. Stoller, K. J. Ganesh, W. Cai, P. J. Ferreira, A. Pirkle, R. M. Wallace, K. A. Cychosz, M. Thommes, D. Su, E. A. Stach and R. S. Ruoff, *Science*, 2011, **332**, 1537–1541.

28 D. K. Padhi and K. Parida, *J. Mater. Chem. A*, 2014, **2**, 10300–10312.

29 X. Zhao, L. Zhang, S. Murali, M. D. Stoller, Q. Zhang, Y. Zhu and R. S. Ruoff, *ACS Nano*, 2012, **6**, 5404–5412.

30 F. Meng, J. Li, S. K. Cushing, J. Bright, M. Zhi, J. D. Rowley, Z. Hong, A. Manivannan, A. D. Bristow and N. Wu, *ACS Catal.*, 2013, **3**, 746–751.

31 Q. L. Yang, S. Z. Kang, H. Chen, W. Bu and J. Mu, *Desalination*, 2011, **266**, 149–153.

32 R. Mu, Z. Xu, L. Li, Y. Shao, H. Wan and S. Zheng, *J. Hazard. Mater.*, 2010, **176**, 495–502.

33 A. Idris, N. Hassan, N. S. M. Ismail, E. Misran, N. M. Yusof, A. F. Ngomsik and A. Bee, *Water Res.*, 2010, **44**, 1683–1688.

34 T. Papadam, N. P. Xekoukoulotakis, I. Poulios and D. Mantzavinos, *J. Photochem. Photobiol., A*, 2007, **186**, 308–315.

35 S. Tuprakay and W. Liengcharernsit, *J. Hazard. Mater.*, 2005, **124**, 53–58.

36 Z. Yan, X. Yu, A. Han, P. Xu and P. Du, *J. Phys. Chem. C*, 2014, **118**, 22896–22903.

37 B. Ahmmad, K. Leonard, M. Shariful Islam, J. Kurawaki, M. Muruganandham, T. Ohkubo and Y. Kuroda, *Adv. Powder Technol.*, 2013, **24**, 160–167.

38 X. Li, X. Yu, J. He and Z. Xu, *J. Phys. Chem. C*, 2009, **113**, 2837–2845.

39 J. Qu, Y. X. Yin, Y. Q. Wang, Y. Yan, Y. G. Guo and W. G. Song, *ACS Appl. Mater. Interfaces*, 2013, **5**, 3932–3936.

40 J. Liu, H. Cao, J. Xiong and Z. Cheng, *CrystEngComm*, 2012, **14**, 5140–5144.